

## Anisotropic Electronic State via Spontaneous Phase Separation in Strained Vanadium Dioxide Films

M. K. Liu,<sup>1</sup> M. Wagner,<sup>1</sup> E. Abreu,<sup>2</sup> S. Kittiwatanakul,<sup>3</sup> A. McLeod,<sup>1</sup> Z. Fei,<sup>1</sup> M. Goldflam,<sup>1</sup> S. Dai,<sup>1</sup> M. M. Fogler,<sup>1</sup> J. Lu,<sup>4</sup> S. A. Wolf,<sup>3,4</sup> R. D. Averitt,<sup>2</sup> and D. N. Basov<sup>1,\*</sup>

<sup>1</sup>*Department of Physics, The University of California at San Diego, La Jolla, California 92093, USA*

<sup>2</sup>*Department of Physics, Boston University, Boston, Massachusetts 02215, USA*

<sup>3</sup>*Department of Physics, University of Virginia, Charlottesville, Virginia 22904, USA*

<sup>4</sup>*Department of Materials Science and Engineering, University of Virginia, Charlottesville, Virginia 22904, USA*

(Received 11 May 2013; published 29 August 2013)

We resolved the enigma of anisotropic electronic transport in strained vanadium dioxide (VO<sub>2</sub>) films by inquiring into the role that strain plays in the nanoscale phase separation in the vicinity of the insulator-to-metal transition. The root source of the anisotropy was visualized as the formation of a peculiar unidirectional stripe state which accompanies the phase transition. Furthermore, nanoscale infrared spectroscopy unveils distinct facets of electron-lattice interplay at three different stages of the phase transition. These stages include the initial formation of sparse nonpercolating metallic domains without noticeable involvement of the lattice followed by an electron-lattice coupled anisotropic stripe state close to percolation which ultimately evolves into a nearly isotropic rutile metallic phase. Our results provide a unique mesoscopic perspective for the tunable macroscopic phenomena in strained metal oxide films.

DOI: [10.1103/PhysRevLett.111.096602](https://doi.org/10.1103/PhysRevLett.111.096602)

PACS numbers: 72.80.Ga, 73.22.-f, 73.23.-b, 78.20.-e

Strain can cause striking new physics in materials with examples that include an increase of the superconducting transition temperature [1], an enhancement of ferroelectric polarization [2], and even giant pseudomagnetic fields in excess of 300 Tesla [3]. Spontaneous formation of polydomains by strain can generate new macroscopic order [4,5], leading to the coexistence of multiple constituent phases in complex materials [6–8]. Transition metal oxides serve as a test bed to investigate strain and phase separation, clarifying the roles of these effects in technologically important phenomena including superconductivity, magnetoresistance and electro-optical switching. With broadband infrared near-field microscopy, we reveal the formation of unidirectional conducting stripes in strained VO<sub>2</sub> films, linked to dramatic conductivity anisotropy and modification of the metal-insulator transition (MIT) temperature  $T_c$ .

The MIT in vanadium dioxide (VO<sub>2</sub>) at 340 K accompanied by a transition from a low temperature monoclinic (*M*) phase to a high temperature rutile (*R*) phase has remained a topic of intense interest since the 1950s [9,10]. One poorly understood aspect of VO<sub>2</sub> physics is the anisotropy of the transition temperature ( $T_c$ ) and dc conductivity in the vicinity of the MIT. In different forms of vanadium dioxide (VO<sub>2</sub>) crystals or films, the degree of electronic anisotropy can range from a factor of 10 to 50 to vanishingly small without any obvious reasons. Such anisotropy was noticed early on [11] but became increasingly apparent with the recent advent of highly ordered crystalline films grown on TiO<sub>2</sub> substrates [12,13]. This is inconsistent with the structure of VO<sub>2</sub> in any of its known crystalline phases [14]. Furthermore, this unusual

anisotropic state is predicted by neither the Mott nor Peierls theories of the MIT, the two leading scenarios invoked to explain the phase transition physics on the basis of electronic correlations and structural transformations, respectively [15,16]. Because meso- and nanoscale phase separation is commonplace in the physics of VO<sub>2</sub>, addressing the anisotropy enigma calls for an exploration of structural and electronic properties at the nanoscale.

Despite rapid progress in the development of scanning probe techniques [17–19], simultaneously probing nanoscale variations of electronic and structural properties over large scanning areas has remained a challenging task. To meet this need, in this work, we employ scattering-type scanning near-field optical microscopy (s-SNOM). Based on an atomic force microscope (AFM), the s-SNOM detects tip-scattered infrared (IR) signals which render local information about the optical properties of the sample surface [17,19]. Signals  $S_n$  demodulated at integer harmonics  $n = 2, 3, 4$  of the fundamental tip tapping frequency are recorded to isolate the genuine near-field contribution to the infrared signal and eliminate additive background artifacts (see the Supplemental Material [20] for further details). Our particular s-SNOM arrangement enables topographic mapping, near-field imaging, and nano-Fourier-transform IR spectroscopy (nano-FTIR) with a spatial resolution down to  $\sim 20$  nm carried out over a broad range of mid-IR frequencies ( $\sim 650$  to  $\sim 2400$  cm<sup>-1</sup>) [21,22]. In addition, we applied a high repetition rate (40 MHz) near-IR ( $\sim 1.56$   $\mu$ m) pump beam focused to a 20  $\mu$ m spot beneath the AFM tip to initiate the MIT in VO<sub>2</sub>. Because of the long recovery time of our VO<sub>2</sub> samples ( $> 25$  ns) in comparison with the laser

repetition rate, the pump beam provides an ultrastable local thermal environment without transient dynamics. Thus, by performing direct pump heating, the AFM measurements are much more stable and the images are sharper at elevated temperatures. With this experimental setup, we observed unidirectional electronic and structural domains in VO<sub>2</sub>, corresponding to real-space signatures of the anisotropic state in the vicinity of the MIT. We identified three distinct stages of the MIT in the temperature range 320–380 K, revealing previously unnoticed aspects of the interplay between structural and electronic transformations in the course of the transition [Fig. 1(a)].

Figure 1(b) displays the temperature-dependent THz conductivity ( $\sigma_{\text{THz}}$ ) of our 300 nm VO<sub>2</sub> film on the [110]<sub>R</sub> TiO<sub>2</sub> substrate, measured by Terahertz time domain spectroscopy (see the Supplemental Material [20] for further details).  $\sigma_{\text{THz}}$  along two different axes ([110]<sub>R</sub> and [001]<sub>R</sub>) was obtained by rotating the film 90° and probing the free-carrier response by polarized THz transmission. The conductivity increase along the [001]<sub>R</sub> axis begins at  $T_{\parallel} \approx 360$  K and proceeds with a sharp and narrow hysteresis. Along the [110]<sub>R</sub> axis, the increase in conductivity onsets at a lower temperature ( $T_{\perp} \approx 320$  K) and the transition trace is unexpectedly broad, with complete metallicity not attained until  $\sim 380$  K. Therefore, VO<sub>2</sub> films on [110]<sub>R</sub> TiO<sub>2</sub> exhibit a dramatically

anisotropic conductivity in the vicinity of the phase transition. This behavior has not been observed in polycrystalline samples, such as VO<sub>2</sub> films grown on a sapphire substrate, confirming the key role of uniaxial strain. The apparent increase in  $T_c$  along the  $c_R$  axis of VO<sub>2</sub> on TiO<sub>2</sub> films has previously been attributed to strain-induced modulation of the electronic bandwidth [15,23] without considering spatial inhomogeneity. As we will show below, in order to understand the data in Fig. 1(b), the underlying physics of strained VO<sub>2</sub> films must be amended by taking proper account of a dominant role of unidirectional phase separation.

Figure 2 presents our central findings: infrared near-field and AFM images of the 300 nm VO<sub>2</sub> film on [110]<sub>R</sub> TiO<sub>2</sub>. The first and second rows of Fig. 2 display infrared near-field ( $S_3$ ) and AFM topography images, respectively. Experiments were performed at room temperature, and the optical pump power was controlled by a neutral density filter (0–25 mW). As shown in the first row in Fig. 2, a highly stripe-ordered pattern with unidirectional domains running along [110]<sub>R</sub> was observed by near-field imaging. The density and width of these stripes gradually increase with increasing pump intensity. Since higher local optical conductivities yield stronger infrared near-field signal (see the Supplemental Material [20] for further details), these near-field images clearly reveal the pump-induced formation of submicron wide metallic stripes. Essentially identical patterns were observed in temperature-dependent imaging experiments (Fig. 2, third row). Comparing light- and temperature-induced changes in our films, we infer that 16 mW of pump power corresponds with a temperature of  $\sim 326$  K, whereas 22 mW corresponds with  $\sim 345$  K.

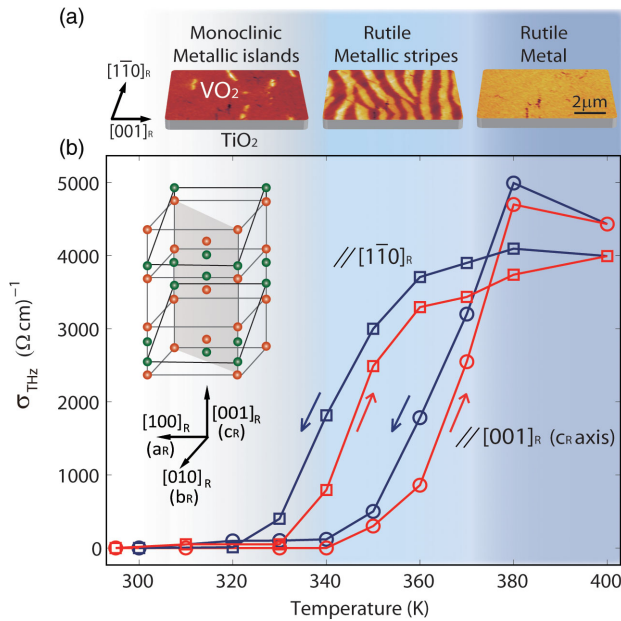


FIG. 1 (color online). (a) Near-field IR images illustrating three distinct stages of the insulator-to-metal phase transition as described in the text. (b) Temperature-dependent THz conductivity ( $\sigma_{\text{THz}}$ ) along the [110]<sub>R</sub> axis (squares) and along the [001]<sub>R</sub> axis (circles). Red (gray) and blue (black) arrows reflect directions of temperature change. Inset: crystal structure of VO<sub>2</sub> in low temperature monoclinic [green (black) spheres] and high temperature rutile [orange (gray) spheres] phases. The shaded plane coincides with the surface of our sample film.

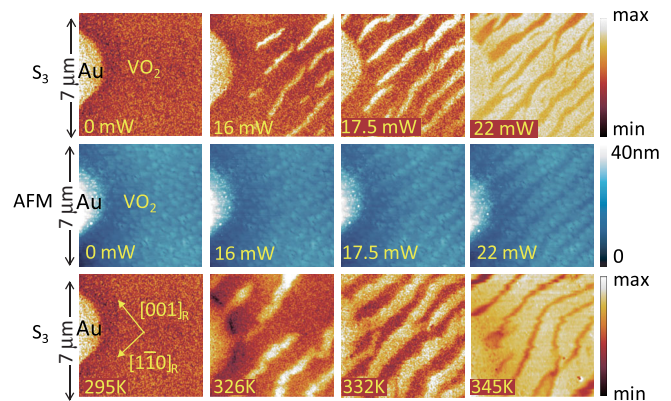


FIG. 2 (color online). Top row: IR scattering amplitude  $S_3$  recorded at distinct power levels of the pump laser. Middle row: sample topography (AFM) for the images displayed in the top row. Bottom row:  $S_3$  images recorded at distinct temperatures. The center frequency of the probe beam used here is  $\sim 1100 \text{ cm}^{-1}$ . The near-field signal in all images is normalized to that from a 50 nm gold film (middle left of each image). Temperature-dependent Raman experiments (not shown) indicate that the monoclinic (M) and rutile (R) phases are coexistent in the temperature range 325–345 K.

AFM images acquired simultaneously with the pump-induced near-field data also show periodic stripe-ordered topographic features (Fig. 2, second row), as will be discussed in detail below. Temperature-dependent Raman experiments (spatially averaged over  $2\ \mu\text{m}$  due to limited optical resolution, not shown) confirmed the coexistence of monoclinic and rutile phases, as observed previously in  $\text{VO}_2$  nanobeams and nanoplatelets [24–27]. Film thickness-dependent studies were also performed to demonstrate the ubiquity of the stripe order in strained  $\text{VO}_2$  films, significantly expanding experimental insights into the stripe state, which until now was only observed in the geometrically confined nanoribbons (see the Supplemental Material [20]).

Figure 2 reveals that the metallic stripes align preferentially along the  $[1\bar{1}0]_R$  axis, thus opening conductive paths along this direction. In contrast, conductivity along the  $[001]_R$  axis is hindered by the intervening insulating domains. Thus, infrared near-field images link the anisotropic conductivity observed by THz measurements (Fig. 1) with a novel mesoscale, unidirectional electronic phase separation (Fig. 2).

The observed transformations in film morphology near the MIT are an entirely novel outcome of our imaging experiments. Figure 3 compares images and corresponding line scans acquired under pump powers of 15 and 20 mW. Simultaneously acquired AFM topography and infrared near-field amplitude ( $S_3$ ) are overlaid to highlight the degree of correlation between the two effects [Figs. 3(a) and 3(b)]. At the initial stage of the phase transition (15 mW, i.e.,  $T \sim 320\ \text{K}$ ), enhancement in the infrared near-field signal shows the formation of sparse metallic nanodomains to be uncorrelated with film topography within our AFM resolution [Fig. 3(c)]. At a later stage

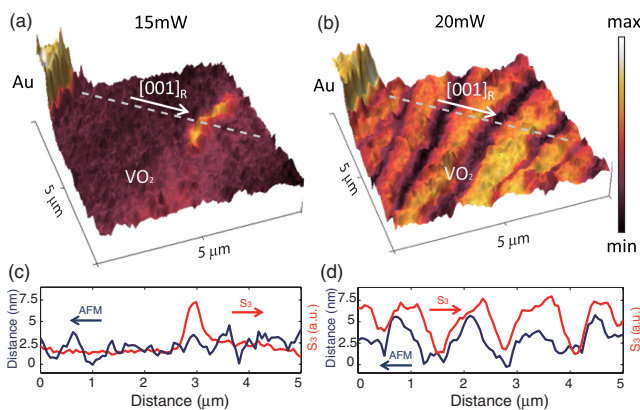


FIG. 3 (color online). (a),(b) The sample morphology (AFM) as a topographic map overlaid with the near-field scattering amplitude signal  $S_3$  as given in the color scale. Corresponding line scans of AFM topography dark blue (black) curves and near-field amplitude red (gray) curves are shown in (c) and (d). Near-field signals are normalized to that from the 50 nm gold film at the upper left corners of (a) and (b).

(20 mW, i.e.,  $T \sim 340\ \text{K}$ ), the density of metallic stripes increases and we observe an unmistakable correlation between infrared near-field amplitude and topographic features; the metallic stripes systematically coincide with height elevations of  $\sim 5\ \text{nm}$  [Fig. 3(d)].

The correlation between infrared amplitude and topography observed at the advanced stages of the MIT is consistent with the notion of a structural transformation in  $\text{VO}_2$  occurring within unidirectional stripes. In order to minimize the strain energy induced by interfacial lattice mismatch, the structural transition occurs in periodic domains oriented along  $[1\bar{1}0]_R$ , allowing part of the film to expand out of plane. It is well known that during the MIT, the rutile  $a_R$  (monoclinic  $b_m$ ) axis expands by  $\sim 0.6\%$  and the  $c_R$  ( $a_m$ ) axis shrinks by as much as  $\sim 1\%$  [28]. In our  $\text{VO}_2$  films, topography elevations indicate an expansion of the  $a_R$  and  $b_R$  axes commensurate with the above expectations. Therefore, the periodic topographic stripes indicate a rutile-monoclinic-rutile structural variation accompanied by a corresponding anisotropy in electronic transport. The periodicity of the stripes decreases with decreasing film thickness, reflecting a competition between the domain interfacial energy and the elastic misfit energy (see the Supplemental Material [20] for further details).

To gain further insight into the interplay between electronic and structural properties across the MIT, we performed spatially resolved nano-FTIR experiments. Figure 4 presents spectra revealing the  $\text{VO}_2$  phonon response at the initial stage of the MIT. After locating a

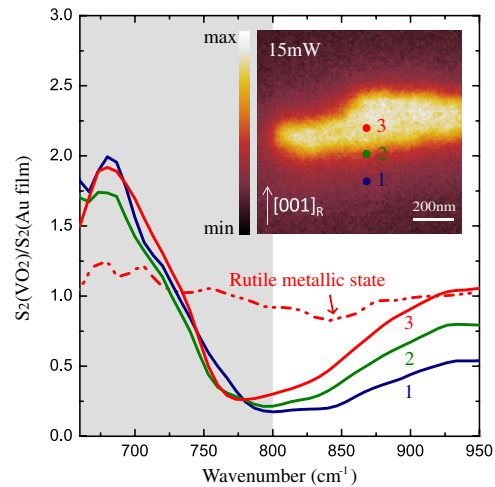


FIG. 4 (color online). Nano-FTIR spectra  $S_2$  normalized to gold and recorded at different positions (1–3) indicated in the inset image of near-field amplitude. The phonon mode of the monoclinic phase of  $\text{VO}_2$  at  $\sim 680\ \text{cm}^{-1}$  can be clearly resolved at all locations 1–3. Note that this phonon peak persists even within the middle of the metallic stripe (3), suggesting a monoclinic metallic state. At higher pump power (20 mW), the monoclinic phonon response disappears at the center of the stripe, signaling a transition to the rutile metallic phase (dash-dotted red curve).

metallic stripe by infrared near-field imaging (inset of Fig. 4), we collected spectra from  $\sim 20$  nm spots at three representative positions. These measurements were performed under 15 mW of optical pump power. The first spectrum collected from the insulating region (1) is dominated by a resonance at  $\sim 680$   $\text{cm}^{-1}$  characteristic of the monoclinic phonon mode of  $\text{VO}_2$  which is known to be absent from the rutile phase [29–33]. Moving closer to the metallic stripe (1  $\rightarrow$  3 series), we observe a gradual increase in the electronic background. At position 3, the electronic background near the high frequency cutoff of our spectra is indistinguishable from that of the rutile phase. Nevertheless, the  $680$   $\text{cm}^{-1}$  hallmark of the monoclinic phase persists throughout all spectra (1–3). For comparison, spectroscopy of the rutile metallic response acquired at the same location at a later stage of the phase transition (20 mW pump power) is also displayed (dashed red line). The  $680$   $\text{cm}^{-1}$  phonon feature is not present in this latter spectrum, attesting to a complete transition into the rutile phase. We remark that the monoclinic metallic islands spontaneously appear across the sample and eventually evolve into metallic stripes. It is therefore unlikely that the nucleation of these initial metallic domains is governed by defects or surface contaminations. Nevertheless, defects smaller than the spatial resolution of our apparatus may play a role in triggering the metallic nucleation.

Our nanoimaging and nanospectroscopy experiments suggest the MIT of strained  $\text{VO}_2$  films proceeds by three distinct stages [illustrated in Fig. 1(a)]. At the initial stage of the phase transition (exhibited by our 15 mW pump power measurements), sparse metallic nucleation occurs without an associated structural transition; this behavior is consistent with Mott physics [15,34–36]. At advanced stages of the phase transition (20 mW pump power, i.e.,  $T \approx 340$  K), the formation of corrugated morphology and the monoclinic-to-rutile structural phase transition stabilize the network of metallic stripes, establishing a highly anisotropic electronic state in strained films. Finally, upon the transition finale ( $\geq 25$  mW,  $\geq 370$  K), the film becomes a uniform rutile metal and exhibits a near-isotropic far-field response.

The infrared near-field imaging and spectroscopy measurements reported here uncover a novel aspect in the mesoscopic properties of  $\text{VO}_2$  which proceeds beyond any single-phase description, offering new insights towards understanding the relationship between  $T_c$ , optical anisotropy, and strain in this prototypical transition metal oxide film. Providing  $\text{VO}_2$  as a case study, here we have demonstrated the unique abilities of infrared near-field imaging and nano-FTIR to resolve and disentangle both structural and electronic phenomena, a crucial requirement for the future advances in the studies of phase transition in complex, phase separated materials [6,37,38]. As a side remark, we mention possible utility of the periodic stripe

pattern revealed by our measurements. This pattern that can be tuned by temperature and light illumination and is also controlled by the sample thickness will produce diffraction characteristics in visible-IR frequencies that can augment current thermo- and electrochromic applications of  $\text{VO}_2$ .

D.N.B. acknowledges support from ARO. Development of nano-optics capabilities at UCSD is supported by DOE-BES. R.D.A. acknowledges support from DOE-BES under Grant No. DE-FG02-09ER46643. M. W. thanks the Alexander von Humboldt Foundation for financial support. E. A. acknowledges support from Fundação para a Ciência e a Tecnologia, Portugal, through a doctoral degree fellowship (No. SFRH/BD/47847/2008). S. K., J. L., and S. A. W. are grateful for the support from the Nanoelectronics Research Initiative (NRI) and VMEC.

---

\*dbasov@physics.ucsd.edu

- [1] J. Locquet, J. Perret, and J. Fompeyrine, *Nature (London)* **394**, 453 (1998).
- [2] J. Wang, J. B. Neaton, H. Zheng, V. Nagarajan, S. B. Ogale, B. Liu, D. Viehland, V. Vaithyanathan, D. G. Schlom, U. V. Waghmare, N. A. Spaldin, K. M. Rabe, M. Wuttig, and R. Ramesh, *Science* **299**, 1719 (2003).
- [3] N. Levy, S. A. Burke, K. L. Meaker, M. Panlasigui, A. Zettl, F. Guinea, A. H. Castro Neto, and M. F. Crommie, *Science* **329**, 544 (2010).
- [4] N. Bowden, S. Brittain, and A. Evans, *Nature (London)* **393**, 146 (1998).
- [5] V. Lyahovitskaya, Y. Feldman, I. Zon, E. Wachtel, I. Lubomirsky, and A. L. Roytburd, *Adv. Mater.* **17**, 1956 (2005).
- [6] T. Z. Ward, J. D. Budai, Z. Gai, J. Z. Tischler, L. Yin, and J. Shen, *Nat. Phys.* **5**, 885 (2009).
- [7] K. Ahn, T. Lookman, and A. Bishop, *Nature (London)* **428**, 401 (2004).
- [8] B. Spivak and S. A. Kivelson, *Ann. Phys. (Amsterdam)* **321**, 2071 (2006).
- [9] F. J. Morin, *Phys. Rev. Lett.* **3**, 34 (1959).
- [10] J. B. Goodenough, *J. Solid State Chem.* **3**, 490 (1971).
- [11] C. Everhart and J. MacChesney, *J. Appl. Phys.* **39**, 2872 (1968).
- [12] J. Lu, K. G. West, and S. A. Wolf, *Appl. Phys. Lett.* **93**, 262107 (2008).
- [13] S. Kittiwatanakul, J. Lu, and S. A. Wolf, *Appl. Phys. Express* **4**, 091104 (2011).
- [14] V. Eyert, *Ann. Phys. (Berlin)* **11**, 650 (2002).
- [15] B. Lazarovits, K. Kim, K. Haule, and G. Kotliar, *Phys. Rev. B* **81**, 115117 (2010).
- [16] S. Biermann, A. Poteryaev, A. I. Lichtenstein, and A. Georges, *Phys. Rev. Lett.* **94**, 026404 (2005).
- [17] A. Huber, A. Ziegler, T. Kck, and R. Hillenbrand, *Nat. Nanotechnol.* **4**, 153 (2009).
- [18] D. Bonnell, D. Basov, M. Bode, U. Diebold, S. Kalinin, V. Madhavan, L. Novotny, M. Salmeron, U. Schwarz, and P. Weiss, *Rev. Mod. Phys.* **84**, 1343 (2012).

- [19] J. M. Atkin, S. Berweger, A. C. Jones, and M. B. Raschke, *Adv. Phys.* **61**, 745 (2012).
- [20] See Supplemental Material at <http://link.aps.org/supplemental/10.1103/PhysRevLett.111.096602> for additional details on the methods and techniques we used in this Letter.
- [21] S. Amarie, P. Zaslansky, Y. Kajihara, E. Griesshaber, W. W. Schmahl, and F. Keilmann, *Beilstein J. Nanotechnol.* **3**, 312 (2012).
- [22] F. Keilmann and S. Amarie, *J. Infrared Millimeter Terahertz Waves* **33**, 479 (2012).
- [23] E. Abreu, M. Liu, J. Lu, K. G. West, S. Kittiwatanakul, W. Yin, S. A. Wolf, and R. D. Averitt, *New J. Phys.* **14**, 083026 (2012).
- [24] J. Wu, Q. Gu, B. S. Guiton, N. P. De Leon, L. Ouyang, and H. Park, *Nano Lett.* **6**, 2313 (2006).
- [25] J. Cao, E. Ertekin, V. Srinivasan, W. Fan, S. Huang, H. Zheng, J. W. L. Yim, D. R. Khanal, D. F. Ogletree, J. C. Grossman, and J. Wu, *Nat. Nanotechnol.* **4**, 732 (2009).
- [26] A. C. Jones, S. Berweger, J. Wei, D. Cobden, and M. B. Raschke, *Nano Lett.* **10**, 1574 (2010).
- [27] A. Tselev, V. Meunier, E. Strelcov, W. A. Shelton, I. A. Lukyanchuk, K. Jones, R. Proksch, A. Kolmakov, and S. V. Kalinin, *ACS Nano* **4**, 4412 (2010).
- [28] D. Kucharczyk and T. Niklewski, *J. Appl. Crystallogr.* **12**, 370 (1979).
- [29] A. S. Barker, Jr., H. Verleur, and H. Guggenheim, *Phys. Rev. Lett.* **17**, 1286 (1966).
- [30] A. Heinrich, E. I. Terukov, W. Reichelt, H. Wagner, and H. Oppermann, *Phys. Status Solidi (a)* **72**, K61 (1982).
- [31] In raw IR reflectance or raw near-field IR scattering data, the apparent width of the phonon feature is determined by the difference between the longitudinal ( $\omega_{LO}$ ) and transverse ( $\omega_{TO}$ ) frequencies. This apparent width can exceed several hundred wave numbers and is ultimately governed by the oscillator strength of the phonon resonance proportional to  $\omega_{LO}-\omega_{TO}$  (see Refs. [29,30]). The genuine width of the phonon mode as a rule is much smaller and can only be estimated from the analysis of the optical constants governing reflectance or scattering data.
- [32] M. M. Qazilbash, M. Brehm, G. O. Andreev, A. Frenzel, P. C. Ho, B.-G. Chae, B.-J. Kim, S. J. Yun, H.-T. Kim, A. V. Balatsky, O. G. Shpyrko, M. B. Maple, F. Keilmann, and D. N. Basov, *Phys. Rev. B* **79**, 075107 (2009).
- [33] T. J. Huffman, P. Xu, M. M. Qazilbash, E. J. Walter, H. Krakauer, J. Wei, D. H. Cobden, H. A. Bechtel, M. C. Martin, G. L. Carr, and D. N. Basov, *Phys. Rev. B* **87**, 115121 (2013).
- [34] M. M. Qazilbash, M. Brehm, B.-G. Chae, P. C. Ho, G. O. Andreev, B.-J. Kim, S. J. Yun, A. V. Balatsky, M. B. Maple, F. Keilmann, H.-T. Kim, and D. N. Basov, *Science* **318**, 1750 (2007).
- [35] H.-T. Kim, Y. W. Lee, B.-J. Kim, B.-G. Chae, S. J. Yun, K.-Y. Kang, K.-J. Han, K.-J. Yee, and Y.-S. Lim, *Phys. Rev. Lett.* **97**, 266401 (2006).
- [36] Z. Tao, T.-R. T. Han, S. D. Mahanti, P. M. Duxbury, F. Yuan, C.-Y. Ruan, K. Wang, and J. Wu, *Phys. Rev. Lett.* **109**, 166406 (2012).
- [37] E. Dagotto, T. Hotta, and A. Moreo, *Phys. Rep.* **344**, 1 (2001).
- [38] S. A. Kivelson, I. P. Bindloss, V. Oganessian, J. M. Tranquada, A. Kapitulnik, and C. Howald, *Rev. Mod. Phys.* **75**, 1201 (2003).